
Article:
Tönnies, F. orcid.org/0000-0002-2287-5815, Brown, A. orcid.org/0000-0002-1623-8086, Kiyim, B. et al. (5 more authors) (2024) Proportional scintillation in liquid xenon: demonstration in a single-phase liquid-only time projection chamber. Journal of Instrumentation, 19 (09). P09032. ISSN: 1748-0221

https://doi.org/10.1088/1748-0221/19/09/p09032

Prepared for submission to JINST

Proportional scintillation in liquid xenon: demonstration in a single-phase liquid-only time projection chamber

Florian Tönnies, Adam Brown, Baris Kiyim, Fabian Kuger, Sebastian Lindemann, Patrick Meinhardt, Marc Schumann

Physikalisches Institut, Universität Freiburg, 79104 Freiburg, Germany

E-mail: florian.toennies@physik.uni-freiburg.de, adam.brown@physik.uni-freiburg.de, marc.schumann@physik.uni-freiburg.de

Abstract: The largest direct dark matter search experiments to date employ dual-phase time projection chambers (TPCs) with liquid noble gas targets. These detect both the primary photons generated by particle interactions in the liquid target, as well as proportional secondary scintillation light created by the ionization electrons in a strong electric field between the liquid-gas interface and the anode in the gas phase. In this work, we describe the detection of charge signals in a small-scale single-phase liquid-xenon-only TPC, that features the well-established TPC geometry with light readout above and below a cylindrical target. In the single-phase TPC, the proportional scintillation light (S2) is generated in liquid xenon in close proximity to 10 µm diameter anode wires. The detector was characterized and the proportional scintillation process was studied using the 32.1 keV and 9.4 keV signals from ^{83m}Kr decays. A charge gain factor g_2 of up to (1.9 ± 0.3) PE/electron was reached at an anode voltage 4.4 keV higher than the gate electrode, corresponding to (29 ± 6) photons emitted per ionization electron. The duration of S2 signals is dominated by electron diffusion and approaches the xenon de-excitation timescale for very short electron drift times. The electron drift velocity and the longitudinal diffusion constant were measured at a drift field of 473 V/cm. The results agree with the literature and demonstrate that a single-phase TPC can be operated successfully.

Keywords: Time projection chamber, liquid noble gas detectors, liquid xenon, electroluminescence

Contents

1 Introduction

Dual-phase (liquid/gas) time projection chambers (TPCs) filled with the liquefied noble gases xenon or argon are widely used in low-background experiments searching for low-energy rare events such as WIMP dark matter [1]. Currently operating detectors with sensitive targets above the tonne scale are PandaX-4T [2], XENONnT [3] and LZ [4], all employing liquid xenon (LXe) targets.

In dual-phase LXe TPCs [5], particle interactions in the LXe target excite and ionize xenon atoms. Subsequent de-excitations lead to a prompt scintillation light signal (S1), that is detected by light sensors installed above and below the cylindrical TPC. Ionization electrons are drifted across the LXe target by means of an electric field, typically around 100 V/cm. This is established between a negatively biased cathode, installed below the LXe target, and a gate electrode (typically at ground potential), just below the liquid-gas interface. A second, stronger electric extraction field ($E \sim 10\,\mathrm{kV/cm}$) established between the gate electrode and the positively biased anode, installed in the xenon gas phase located a few millimeters above the liquid surface, extracts the electrons into the gas phase where they create electroluminescence photons. This secondary light signal (S2) is proportional to the number of electrons. The photons from both processes release photoelectrons (PE) in the photosensors that create the recorded signal. The ratio of detected photoelectrons to

photons produced in the S1 is given by the gain factor g_1. The electroluminescence yield describes the number of secondary photons created by a single electron extracted into the gas. The gain factor g_2 combines this with the detection efficiency to give the number of detected photoelectrons per electron. Typical g_2 values of current dual-phase experiments range from about 15 to almost 50 PE/electron [6–8]. The position of the primary interaction in the TPC can be inferred from the pattern of the detected S2 signal across the top photosensors (xy) and by the time difference between S1 and S2 signal (z). The number of individual S2 signals, indicating the scatter multiplicity, and the ratio S1/S2 can be used to separate dark matter signals from background events.

Although dual-phase LXe TPCs currently provide the tightest constraints on WIMP dark matter interactions for WIMP masses above about 3 GeV/c^2 [1], the technology faces experimental challenges. All TPC electrodes have to be highly optically transparent to enable light detection; they are typically made from individual parallel wires [9], two-dimensional (etched or woven) meshes [4, 10], or – in case of cathode and anode – solid quartz-plates with a conductive layer [11]. The size of the S2 signal depends on the electron path length in the xenon gas and the local electric field, and no S2 signal is produced in regions where the anode touches the liquid-gas interface. This means the gate electrode and anode have to be precisely positioned, parallel to each other and to the liquid-gas interface, for a uniform detector response. The liquid level also needs to be kept stable over long time periods. Due to the combination of electrostatic and gravitational forces, a position-dependent deflection of the anode and gate planes cannot be avoided, which requires position-dependent corrections to the S2 signal [9, 10]. To minimize this effect and prevent the anode from touching the liquid-gas-interface, the electrodes wires or meshes must be tensioned. This implies more massive support frames for the wires, leading to increased radioactivity and associated background.

Creating the proportional S2 scintillation signal in the liquid xenon phase overcomes these issues. However, an electric field greater than ~400 kV/cm is required for the electron to excite xenon atoms. Such fields can be created in the $E(r) \propto 1/r$ radial field close to the surface of thin anode wires [12]. However, excessively high fields result in electron multiplication, worsening the energy resolution [13].

Due to the absence of the liquid-gas interface, proportional scintillation in the liquid phase also prevents the delayed extraction of electrons into the gas phase, which contribute significantly to the accidental coincidence background of current dual-phase TPCs [7, 14]. Total internal reflection on the liquid-gas interface is also avoided, increasing the S1 photon detection efficiency by 5% absolute [15].

Proportional scintillation in liquid xenon was first observed in proportional scintillation counters around thin wires [16, 17]. More recently, the technology regained attention for dark matter searches [12]. Aprile et al. studied 5.4 MeV signals from ^{210}Po α-decays in a small cubic TPC prototype with a 5 mm a drift region and one single anode wire; the light was recorded by two photomuliplier tubes, one above and one below the target [18]. Charge yields of up to 1.8 PE/electron have been achieved in a novel geometry: the radial TPC [19], where a single thin anode wire is centrally located in a cylindrical liquid xenon volume [19, 20].

In this work we demonstrate proportional scintillation in liquid xenon in a standard cylindrical TPC, i.e., a small-scale version of current dark matter TPCs, which has previously been operated and characterized in dual-phase mode [21]. The etched hexagonal anode mesh of the dual-phase detector

was replaced by a set of parallel, 10 µm wires, while the rest of the TPC remained untouched.

In Section 2 of this work we describe the design and operation of the small-scale single-phase TPC on the XeBRA detector platform. This provides a cryostat and a cooling system that can accommodate LXe detectors of a few kilograms, a system for gas storage and purification, as well as data acquisition (DAQ) and slow control systems. The detector is characterized and the proportional scintillation in liquid xenon is studied using low-energy ^{83m}Kr-events. The data analysis and signal corrections are presented in Section 3. We report on our results, in particular the electroluminescence gain and the duration of the observed S2 signals, in Section 4.

2 Design and operation of the single-phase TPC

2.1 Time Projection Chamber

The dual-phase TPC presented in [21] was modified to operate it in single-phase mode, and is shown in Figure 1. The TPC is contained in a vacuum-insulated double-walled cryostat, filled with about 10 kg of xenon. Roughly 0.75 kg of LXe are contained in the cylindrical active TPC volume, where interactions can be detected. This volume has a height of 70 mm, between the cathode and gate electrode, and an inner diameter of 70 mm. These dimensions reduce to 69 mm at LXe temperature. One Hamamatsu R11410-10 PMT of 3-inch diameter is installed below the active volume. The PMT is surrounded by a solid aluminium displacer to reduce the total required amount of LXe. Seven 1×1-inch Hamamatsu R8520 PMTs detect the light distribution across the top of the TPC which can be used to infer the horizonal xy-position of an interaction from the S2-signal, as described in Section 3.4.

For the single-phase operation, a new anode electrode was manufactured. It consists of a set of parallel California Fine Wire gold-plated tungsten wires of 10 µm diameter. This diameter leads to surface electric fields of 730 kV/cm to 1220 kV/cm at anode voltages of 3 kV to 5 kV relative to the surroundings. The wires were stretched across a circular stainless steel frame by fixing one end of the wire between the frame and a copper washer using stainless steel M2.5 bolts, see Figure 2. The other end was tensioned with a 20 g weight and then also fixed. The resonant modes of all wires on the finished anode were measured and from these the individual wire tensions were found to range from 30 to 180 mN. The performance of the individual wires were not observed to depend on their tension.

While the anode frame can accommodate wires at a pitch of 5 mm, only every second wire was installed, since this is expected to lead to higher and more regular fields around the anode wires [13]. The anode wire pitch is thus 10 mm and six anode wires cover the cross section of the TPC. A stainless steel cover placed on top of the bolts avoids high-field regions around sharp edges.

The gate and screening electrodes are installed 5 mm below and above the anode, respectively, with precision-machined PTFE rings as spacers. They and the cathode electrode,installed 70 mm below the gate electrode, are hexagonal stainless steel meshes. These are etched from a 150 µm thick stainless sheet and feature a 3 mm pitch and a web width of 150 µm. The voltages of cathode, gate electrode and anode can be set independently to establish the electric drift and proportional scintillation fields. The active volume of the TPC is enclosed by a PTFE tube of 70 mm inner diameter. A set of five copper field shaping rings, connected by high-ohmic resistors, are located

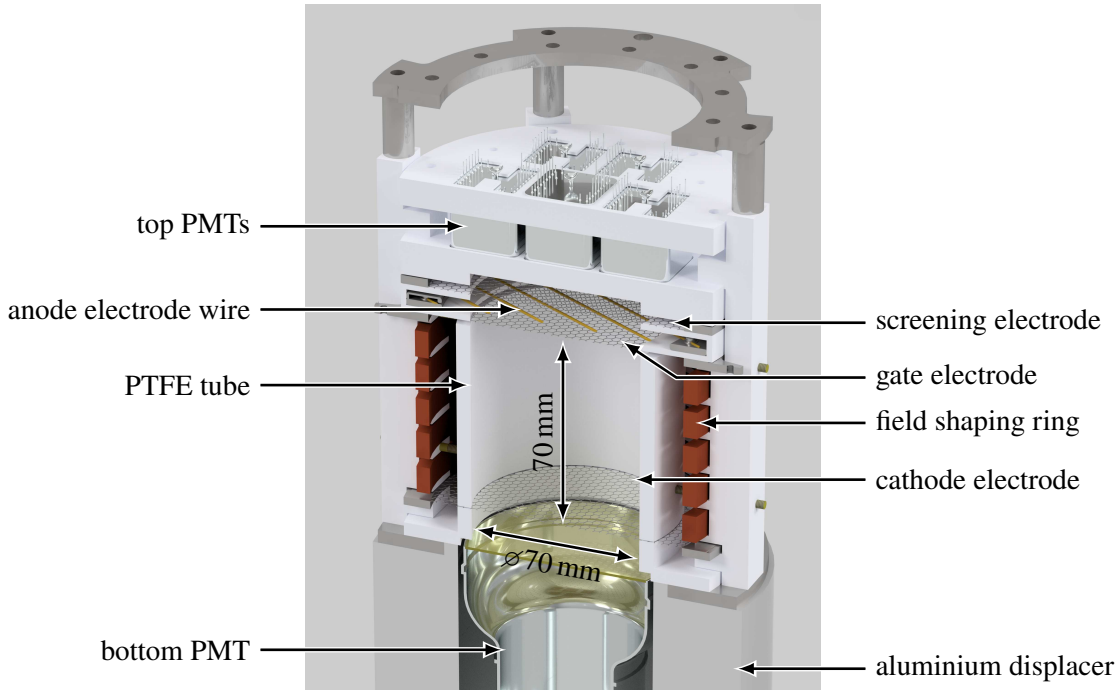

Figure 1. 3D-rendering of the single-phase TPC. The dimensions are specified for room temperature. The anode wires of 10 µm diameter are enlarged for visibility.

Figure 2. CAD image of the anode electrode. The gold-plated tungsten wires of 10 µm diameter are fixed to the stainless steel support frame by means of copper washers and stainless steel bolts. To increase visibility, the wire diameter is enlarged in the image. By using every second wire position, a 10 mm wire pitch is achieved. Only half of the stainless steel piece to cover the screws is shown.

10 mm outside the inner surface of the PTFE tube. This separation, relatively large compared to the radius of the TPC, improves the field homogeneity inside the TPC. Further details about the detector and the XeBRA platform can be found in [21].

2.2 Operation

The cryostat was filled with about 10 kg of liquid xenon such that the top PMTs were partially submerged. For single-phase operation, neither precise liquid level control nor leveling are required. The detector was operated stably using a liquid-nitrogen based cooling system [21] with the gaseous xenon being kept at 1.7 bar absolute pressure and a temperature of 174 K. During operation the xenon was purified by a SAES MonoTorr PS3-MT3-R-2 hot getter. Liquid xenon was extracted from the region outside the TPC via a custom-built heat exchanger and pushed back into the TPC below the cathode. Any returning gaseous xenon which was not liquefied in the heat exchanger was directed to the cold finger located in the gas phase above the detector to be liquefied. The purification system also allowed injecting ^{83m}Kr atoms into the TPC for detector calibration.

The PMT signals were amplified by a factor of 10 by custom amplifiers built for the XENONnT experiment. The data acquisition system is also based on the triggerless system developed for XENONnT [22]. It independently digitizes every PMT waveform exceeding a threshold of 20 mV (equivalent to) using a CAEN V1724 ADC with 14 bit resolution over a 2.25 V dynamic range and 100 MHz sampling frequency. Every PMT waveform includes two samples from before the threshold is crossed and 15 samples after dropping below the threshold again. One of the 7 PMTs in the top array did not operate at cryogenic temperatures, most likely due to a faulty cable connection. The Doberman slow control system [23], specially developed for such small- to medium-scale experiments, was used to operate the system stably for several weeks.

Data were taken with varying amplification fields for proportional scintillation. The voltage ΔV_{ag} of the anode above the gate and screening electrodes was increased in steps of 200 V from 3.0 kV to 5.0 kV. The gate and screening electrodes were always held at the same voltage at each other. For each value of ΔV_{ag}, data were recorded with two different gate and screening electrode voltages of −1 kV and −2 kV. As no difference could be observed in the data from each of these two absolute voltages, all data for a given ΔV_{ag} are combined in the analysis presented here. The cathode voltage was set to either −4.5 kV or −5.5 kV to maintain a potential difference of 3500 V across the 69 mm long drift region. The electric drift field E_d inside the active region was calculated using finite element simulations, taking into account the detailed geometry. The median field strength is $E_d = 473\,\mathrm{V/cm}$, with a one-sigma spread of 8 V/cm. The drift time of electrons produced at the cathode was 42 µs. This is shorter than the average electron lifetime $\tau_e \approx 80\,\mu\mathrm{s}$ caused by the residual electronegative impurities in the LXe (see section Section 3), meaning most electrons released in an interaction reach the anode.

Data could be acquired at eight different amplification fields ΔV_{ag}. Below $\Delta V_{\mathrm{ag}} = 3.4$ kV, very few S2s could be identified due to their small signal, leading to a large statistical uncertainty. Above $\Delta V_{\mathrm{ag}} = 4.4$ kV a constant, high rate of very small signals of unknown origin occupied the digitizer channels and prevented the recording of a sufficiently large number of events with identifiable S1-S2 pairs. A previous attempt to operate the single-phase TPC was limited to even lower anode voltages. Before taking the data used in this work, a careful cleaning campaign was followed in a cleanroom to remove dust from the TPC. Nevertheless, since the XeBRA facililty itself is not in a cleanroom, some dust exposure was unavoidable.

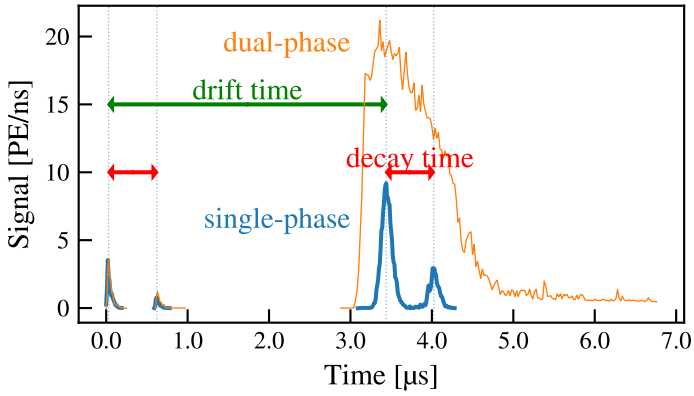

Figure 3. Example ^{83m}Kr events measured with the single-phase TPC (blue) and the same TPC operated in dual-phase mode (orange, from [21]). For direct comparison events with similar drift and decay times were selected and plotted together. The decay time is indicated by the red arrows, the drift time is marked by the green arrow. Both signals feature the characteristic double-S1 pattern of the ^{83m}Kr decay while the corresponding two S2 signals can only be clearly identified in the single-phase TPC. This is due to the different mechanisms to produce the proportional scintillation S2 light.

3 Data analysis

The TPC was characterized and the production of proportional S2 signals in the liquid xenon phase was studied using a ^{83m}Kr conversion electron source [24, 25]. It decays in two steps, which produce electronic recoil signals of 32.1 keV and 9.4 keV energy and have mean lifetimes of $\tau_1 = (2.64 \pm 0.02)$ h and $\tau_2 = (226 \pm 7)$ ns, respectively. The delayed-coincidence decay provides a signature which is easily identified in an unshielded, high background environment. Both decays produce an S1 with an accompanying S2, so that four signals are visible in the TPC. The time difference between the S1 and the S2 from each decay depends on the depth of the decay in the TPC. The time difference between the two S1 peaks (and the two S2 peaks) is given by the decay time of the intermediate ^{83m}Kr state.

Two example ^{83m}Kr events with this structure, acquired during the dual- and the single-phase operation of the same TPC, are shown in Figure 3. The S2 signals from the single-phase TPC are much shorter, because the S2 light is created close to the anode wires [13]. In this example, the two S2 signals are merged due to their duration. More details on S2 duration in the single-phase TPC are presented in Section 4.4.

3.1 Event selection

The strax framework [26], developed by the XENON dark matter collaboration [14], is used to process the raw data. In this framework, a hit is an excursion of the digitized waveform from a single PMT above a pre-defined threshold, which is set slightly above the baseline. The area of a hit is expressed in photoelectrons (PE) by dividing its area by the gain of the PMT. The statistical method described in [27] was used to monitor the gain in regular calibrations, in which the emission of a few PEs was stimulated by pulsed LED light. Hits are merged into peaks based on their

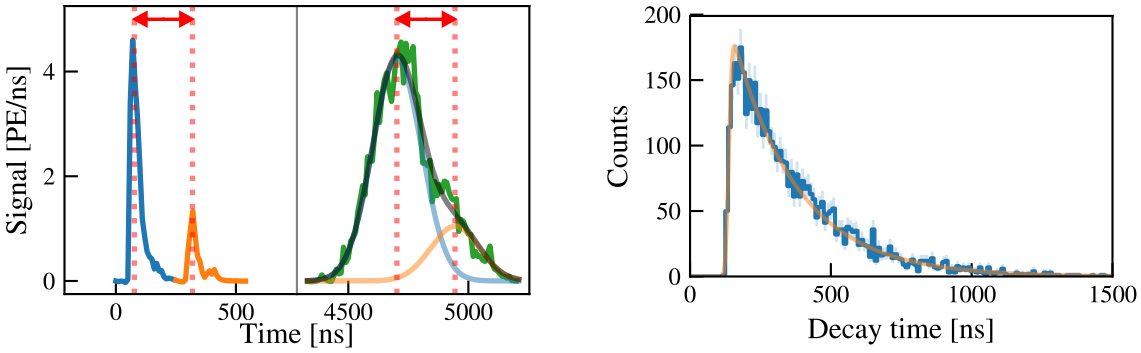

Figure 4. **Left:** S2 fitting procedure applied to a ^{83m}Kr decay where the two S2 signals have significant overlap. The time difference between the two Gaussians used to fit the combined S2 peak is fixed to the time difference between the two S1s. **Right:** The decay time distribution of the ^{83m}Kr events selected for the analysis presented in this work. A fit of an exponential function multiplied by an error function to the data yields a ^{83m}Kr lifetime of (230 ± 5) ns. The mid-point of the error function is at (139.6 ± 1.2) ns and corresponds to the minimum decay time to separate the two S1 peaks.

temporal proximity. Peaks occurring within 120 µs of each other are grouped into an event. This interval is chosen such that all peaks resulting from a single interaction are in the same event.

For the analysis presented here, signal purity is more important than statistics. Only events with at least three peaks with areas above 25 PE are considered as potential ^{83m}Kr events and used for further analysis. The first two peaks in an event are always attributed to the two ^{83m}Kr S1s, the following peaks to S2s. If only three peaks are present in an event, it is assumed that the two S2s were merged into a single peak due to a combination of a short decay time and electron diffusion. If four or more peaks are present, the third and fourth peak are assumed to be the two S2s, provided that the time between them is not more than 50 ns different from the time between the two S1s. If the time differs by more than this, the fourth peak is assumed to be a spurious signal such as an afterpulse, and the third peak is considered to be the two combined S2s. Any further peaks after these are ignored. In all cases, a sum of two Gaussian functions is fitted to the waveform containing the S2 candidates. An example of such a fit is shown in Figure 4, left. The time between the centers of the Gaussians is fixed to the decay time obtained from the S1 peaks. The areas and widths of the Gaussians are left free in the fit. The fit is used to obtain the individual S2 areas, their durations, and the event's drift time, given by the temporal distance of the first S1 peak to the mean of first S2 peak. This fitting procedure enables the use of events where the S2s are relatively close in time. In these cases a more conventional approach, where the peak would be split into two parts at a certain time, could result in biased estimates of the individual S2s' areas.

Several criteria ensure the purity of the ^{83m}Kr sample. Both S1s are required to have an area between 25 PE and 250 PE. The S2 area must be between 25 PE and 60 000 PE, which is loose enough to avoid rejecting good events at high or low anode voltages ΔV_{ag}. Additionally, the time difference between the two krypton decays must be smaller than 1.5 µs, which cuts only 0.1% of all krypton decays. No lower threshold is set for the time difference. However, due to the duration of the individual S1 signals, only ^{83m}Kr events with a decay time of at least 140 ns can be separated by our analysis procedure, as seen in Figure 4, right. This means that only around half of all

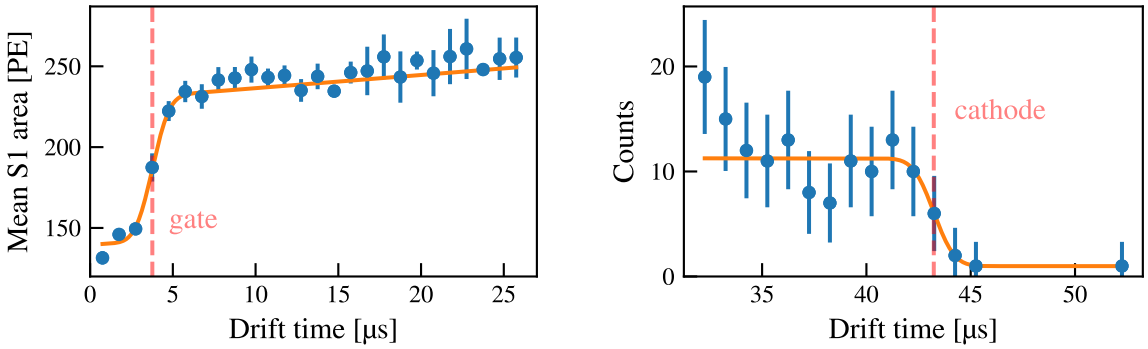

Figure 5. The drift time of events from the gate electrode (left) and cathode (right) are obtained by identifying the steps in the S1 signal size and count rate, respectively. In each case, an error function is fitted to the binned data and the midpoint is taken to correspond to the drift time from that electrode. In the case of the gate electrode this is $T_g = (3.76 \pm 0.14)$ µs, and for the cathode it is $T_c = (43.2 \pm 0.6)$ µs.

^{83m}Kr events are used for the analysis. Figure 4, right, also demonstrates the purity of the selected ^{83m}Kr sample: the lifetime extracted from the exponential fit is (230 ± 5) ns, which agrees with the literature value of (226.2 ± 0.7) ns [28].

3.2 Fiducialization

A homogeneous drift field is required to ensure uniform signal generation. Leakage through the cathode and gate electrode affects the field in their vicinity. To cut these regions from the data, the same procedure is used to identify the drift times corresponding to the gate electrode and cathode positions as presented in [21]. As the electric field is different below and above the gate electrode, recombination and therefore the S1 area are different. This effect is used to identify the drift time of the gate electrode, as seen in Figure 5 (left), where the mean area of the S1 signal is shown as a function of the drift time. The dependence is described by an error function multiplied by a linear term to represent the drift-time dependent light collection efficiency. The drift time at 50% of the error function is taken as the drift time of the gate electrode T_g. Below the cathode, the field is reversed and therefore no S2 signals are seen from decays occurring there. The drift time of the cathode T_c is found by fitting the number of events as a function of the drift time with an error function, as seen in Figure 5 (right).

The drift time is corrected by subtracting T_g, to obtain only the drift time within the region below the gate electrode. Effects which occur while electrons drift from the gate electrode to the anode are considered to be an intrinsic part of the S2 light generation technology. Fiducialization in depth (z) is performed by keeping only events with corrected drift times between 5 µs and 35 µs, corresponding to 8.8 mm and 61.6 mm below the gate electrode. A radial fiducial cut is not applied for this analysis. This is because the drift field is uniform up to the TPC radius of 35 mm due to the large 10 mm distance between the inner PTFE surface and the field shaping electrodes [21]. Optical simulations show that the dependence of the S1 signal on the radial position is minimal and can be neglected [29].

3.3 Corrections

To compensate for the depth-dependent light collection efficiency caused by the geometry of the TPC, a linear fit to the mean measured S1 area as a function of the corrected drift time is performed, as seen in Figure 6, left. S1 signals are corrected with this function to achieve a homogeneous response, using the center of the drift region as reference position. The corrected signal is denoted cS1.

Electronegative impurities such as oxygen or water can absorb electrons drifting towards the gate electrode. This reduces the observed S2 signal depending on the depth of an event. The exponential loss of electrons is described by the so-called electron lifetime. It is extracted from the data by taking all ^{83m}Kr events in a drift time bin and performing a Gaussian fit on the area distribution of the first S2 to obtain the mean signal. An exponential function is fit to this mean area as a function of the drift time is performed, as seen in Figure 6, right. An electron lifetime of 80 µs was achieved during the measurements used for this work, which is about twice the maximal drift time. To compensate for the charge loss, the S2 signals are scaled towards the gate electrode using the electron lifetime to obtain the corrected S2 signal cS2.

After selecting and correcting the ^{83m}Kr data, the four characteristic signals populate distinct regions in a space defined by the signal duration and the corrected signal area, as shown in Figure 7. The duration is defined as the interval between the 25% and 75% quantiles of the peak. The duration can be used to classify signals as S1 or S2. Further information on signal classification is given in Section 4.5.

3.4 Position reconstruction

The results of this work do not require radial fiducialization since ^{83m}Kr events can be identified with minimal backgrounds and thanks to the small radial dependence of the single-phase TPC response. Nevertheless, the ability of the single phase TPC to reconstruct the horizontal (xy) position of events based on the distribution of the S2 light signal across the 1 × 1" photomultipliers in the top array was studied.

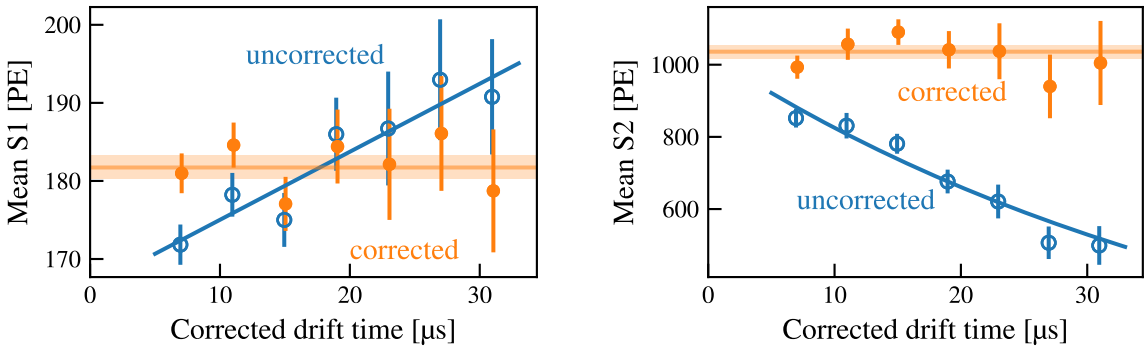

Figure 6. Corrections of the S1 and S2 signals. **Left:** Monoenergetic S1 signals are impacted by the z-dependent light collection efficiency, which can be described by a linear function (blue). The function is used to correct the S1 areas towards the center of the TPC volume (orange). **Right:** The drift-time dependent S2 charge signal loss to electronegative impurities can be described by an exponential function (blue). The S2 signals are corrected using this function towards the gate electrode position (orange).

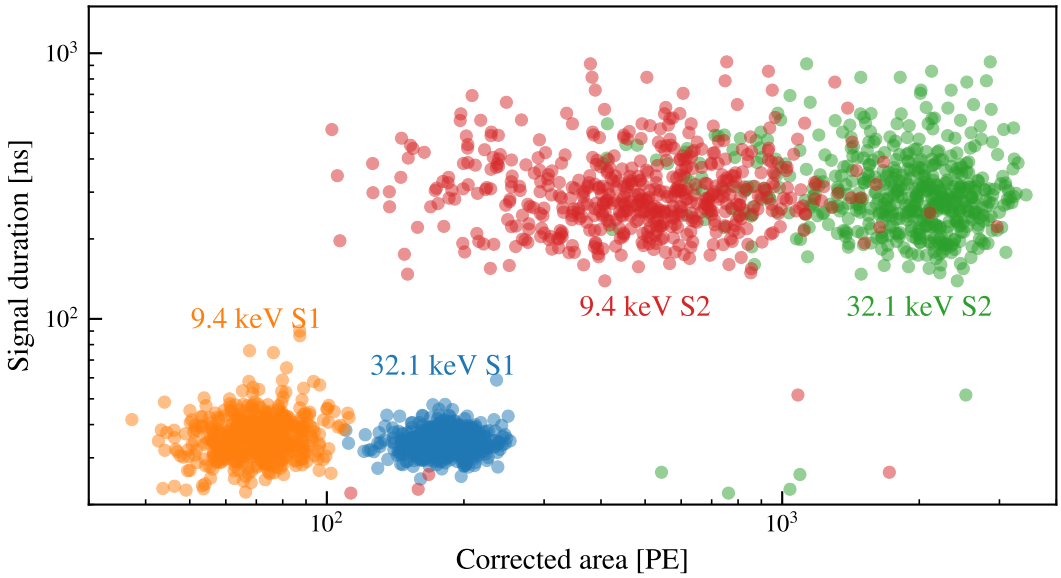

Figure 7. The four S1 and S2 signals of ^{83m}Kr events inside the fiducial volume for an anode to gate electrode voltage difference of $\Delta V_{ag} = 4.4\,\text{kV}$. The S2 signals (green and red) are wider and larger than the S1s (blue and orange).

The reconstruction of the horizontal events position makes use of a deep feed forward neutral network, trained with the light response. This light response in the single-phase TPC was simulated using GEANT4 [30]. The neural network is built using TensorFlow [31], accessed via the Keras API [32]. The input layer of the neural net is given by the relative signals of the seven top array PMTs. This is connected to the output layer, consisting of the two horizontal positions x and y, via two hidden layers with 64 nodes each. Since proportional scintillation in the liquid xenon happens only very close to the wires [13], the network is trained by randomly generating 20,000 events along each of the six anode wires. Each event consists of 1000 individual photons, which are created in a cylinder of 20 µm radius around the 10 µm wire. The relative orientation Φ of the anode wires, which extend along the y-coordinate, to the top PMT array was not precisely measured and was only known to be in the range 30° to 50°. An angle $\Phi = 40°$ is used here. One of the outer PMTs in the top array was not operational during data taking and is thus not used for the training.

The reconstructed positions of events acquired at all ΔV_{ag} are shown in Figure 8, left. The reconstruction artifacts and the slight asymmetry are partly due to the non functional PMT. To quantify the reconstruction quality, the reconstructed positions of the the S2s from the two ^{83m}Kr decays are compared. Thanks to the high efficiency of tagging ^{83m}Kr events and the short time between the two decays, these are known to come from the same position. The distribution of the difference between the two reconstructed positions, where each decay is reconstructed separately, is shown in Figure 8, right. The median difference between the positions is 7 mm, and is representative of the position reconstruction resolution. This is compared to the distance between randomly paired S2s, which are expected to be uncorrelated. For these randomly paired decays, the median distance is 32 mm, close to half the TPC diameter.

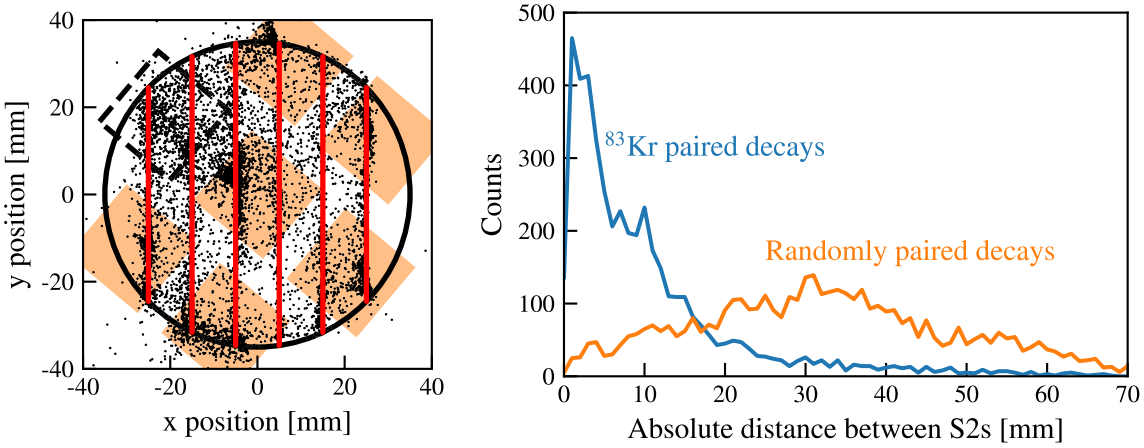

Figure 8. Horizontal position reconstruction in the single phase TPC. **Left:** Reconstructed event positions along the six anode wires (red lines) which were used to define the coordinate system. The quadratic photocathodes of the top array PMTs, which are rotated by $\Phi \approx 40°$ with respect to the wires, are shown in the background (light orange). The black circle denotes the reflective PTFE wall. The PMT located at $(x, y) = (-21, +18)$ mm was not operational. **Right:** The distance between the reconstructed positions from each of the two decays of a ^{83m}Kr nucleus, with a median of 7 mm, in blue. This is compared to randomly paired events, in orange, with a median of 32 mm.

4 Results

Single-phase data of good quality could be acquired at eight anode-gate voltage differences ΔV_{ag} between 3.0 kV and 4.4 kV, and at two absolute gate and screening electrode voltages of -1 kV and -2 kV. At higher ΔV_{ag} spurious light emission severely affected data taking. The drift field was kept constant for all measurements. The 32.1 keV and 9.4 keV decays of ^{83m}Kr were used to measure the scintillation yield, energy resolution and other characteristics of the single-phase TPC.

4.1 Electron drift velocity

Using the drift time from the cathode T_c and gate electrode T_g and the cathode-gate distance of $\Delta z = 69$ mm at LXe temperature, the electron drift velocity can be determined as $v_D = \Delta z/(T_c - T_g) = (1.75 \pm 0.03)$ mm/µs at the drift field of 473 V/cm. The uncertainty is dominated by the errors on T_c and T_g. This value agrees with other recent measurements [21, 33].

4.2 Secondary scintillation yield

The equation

$$E = W\left(\frac{\mathrm{cS1}}{g_1} + \frac{cS2}{g_2}\right) \tag{4.1}$$

relates the energy E of the two krypton decays at 32.1 keV and 9.4 keV to the corrected S1 and S2 areas. The constant $W = 13.7$ eV is the average xenon excitation and ionisation energy [34]. The gain factors g_1 and g_2, for the S1 and S2 signals, respectively, give the number of photoelectrons detected per quantum produced, after signal corrections are applied. They can be determined from

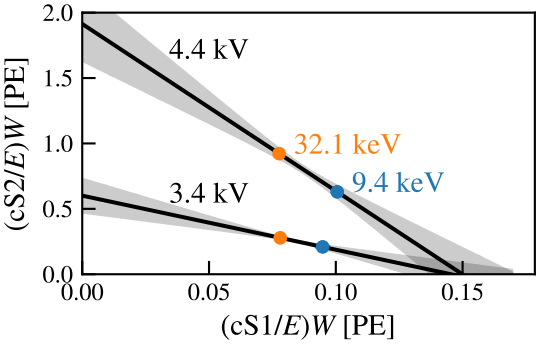

Figure 9. Fit to the light and charge signals at ΔV_{ag} = 3.4 kV and 4.4 kV to obtain the g_1 and g_2 gain factors.

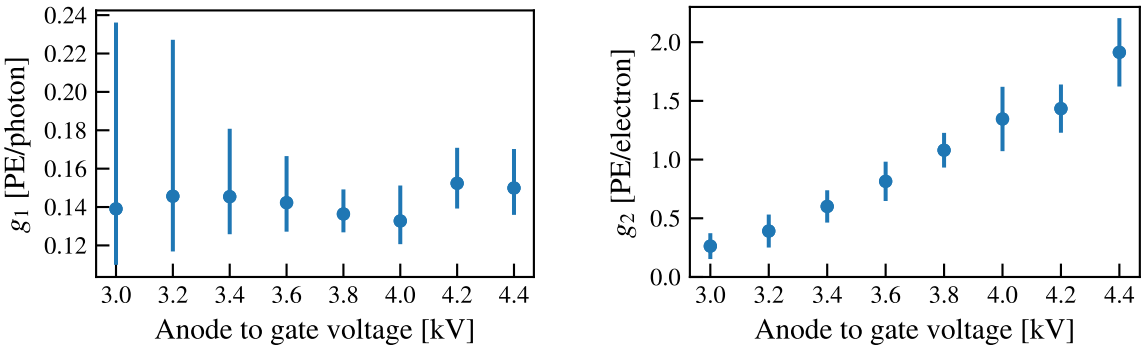

Figure 10. The gain factors g_1 and g_2 for increasing anode-gate voltages ΔV_{ag}. Since the drift field is constant, g_1 (left) does not change with increasing ΔV_{ag} while g_2 (right) increases up to (1.9 ± 0.3) PE/electron.

a linear fit to the corrected signals cS1 and $cS2$ as shown in Figure 9 for ΔV_{ag} = 3.4 kV and 4.4 kV. Only ^{83m}Kr events with decay times larger than 600 ns are used to determine g_1 and g_2. For shorter decay times, the electrons from the first decay impact the local electrical field, resulting in a different charge yield for the second decay [35, 36].

The gain factors are determined independently for all studied voltages ΔV_{ag}, as seen in Figure 10. As expected, g_1 is independent of ΔV_{ag}, as the light is produced in the active TPC target, unaffected by the anode voltage. The individual measurements are thus averaged to g_1 = (0.142 ± 0.008) PE/photon. This value is slightly higher than the (0.122 ± 0.002) PE/photon obtained in the dual-phase version of the TPC [21]. This is explained by the absence of the liquid-gas interface, which can cause total internal reflection and a second pass of the light through the gate electrode in dual-phase operation, and by the higher optical transparency of the anode. The ΔV_{ag}-dependence of the charge gain g_2 is shown in Figure 10, right. It is consistent with the expected exponential increase and ranges from (0.26 ± 0.11) PE/electron at 3.0 kV to (1.9 ± 0.3) PE/electron at 4.4 kV.

The analysis was repeated for ^{83m}Kr events with drift times shorter than 2.5 µs, i.e., above the fiducial target selected above, to estimate the photon detection efficiency for S1 signals in a region close to the anode, where the proportional S2 signals are created. Uncorrected signals were used: the S1 correction is not applied in order to measure the absolute local light yield and the S2 correction is not required as the high electron lifetime and the short drift time result in fewer than

4% of electrons being absorbed by impurities. Runs with ΔV_{ag} from 4.0 kV to 4.4 kV were grouped together to increase statistics. Using the procedure above yields a photon-detection efficiency close to the anode region of $g_1^{\mathrm{a}} = (0.091 \pm 0.013)$ PE/photon. By dividing the S2 gain g_2 by this value, we can determine the detectable electroluminescence gain, or the number of detectable photons created per electron reaching the anode wire. At the highest anode voltage $\Delta V_{\mathrm{ag}} = 4.4$ kV, this is (21 ± 4) photons/electron.

A model for the electroluminescence gain has been proposed by Aprile et al. [18]. The charge gain, for a step size Δr at a distance r from the center of an anode wire, relates the increase in the number of electrons ΔN_{e} to the current number of electrons N_{e}:

$$\Delta N_{\mathrm{e}} = N_{\mathrm{e}} \Theta_0 \exp\left(-\frac{\Theta_1}{E(r; \Delta V_{\mathrm{ag}}, d_{\mathrm{w}}) - \Theta_2}\right) \Delta r. \tag{4.2}$$

The charge gain is described by the three parameters $\Theta_{0,1,2}$, where Θ_2 acts as a threshold field above which amplification is possible, and depends on the electric field $E(r; \Delta V_{\mathrm{ag}}, d_{\mathrm{w}})$. The field is in turn a function of the anode-gate voltage and the wire diameter d_{w}. Using the values for Θ_i from [18], the total charge multiplication factor is about 1.4 for the highest ΔV_{ag} considered here. The number of electrons is then used to calculate the number of photons ΔN_γ generated in each step, where the parameters Θ_3 and Θ_4 describe the proportional scintillation per electron and Θ_4 is the threshold for electroluminescence:

$$\Delta N_\gamma = N_{\mathrm{e}} \Theta_3 \left(E(r; \Delta V_{\mathrm{ag}}, d_{\mathrm{w}}) - \Theta_4\right) \Delta r. \tag{4.3}$$

Each formula is valid only when the electrical field is larger than the threshold, otherwise the gain in that step is zero.

As the S2 light creation happens within a few micrometers to the anode wire [13], a fraction of the photons hits the wire and possibly escapes detection. By including the geometrical coverage of the wire at each step in the model, the fraction of lost photons can be determined under the assumption of zero reflectivity. Correcting for this, the detectable electroluminescence gain quoted above increases to an emitted electroluminescence gain of (29 ± 6) photons/electron at $\Delta V_{\mathrm{ag}} = 4.4$ kV.

A direct fit of the light production model given in (4.2) and (4.3) to our data was not possible because the data do not cover a sufficiently large ΔV_{ag} range to constrain the parameters. However, the Θ_i parameters for the 10 µm wire from [18] result in a model which is compatible with our data after solving iteratively. The electric field $E(r; \Delta V_{\mathrm{ag}}, d_{\mathrm{w}})$ needed for this model was obtained using finite element method simulations of the anode electrode installed in our TPC.

The electroluminescence yield from our single-phase TPC is shown in Figure 11 and compared to the model. Increasing Θ_4 in (4.3), which represents the threshold for proportional scintillation in LXe, by 15% to $\Theta_4 = 460$ kV/cm yields a better fit to our data. This value is close to the 465 kV/cm found in a recent work on proportional scintillation in liquid xenon around microstrips [37]. For comparison, we also show the electroluminescence gains obtained by Qi et al. [20] and Aprile et al. [18], also for 10 µm wires. In the latter case, we use the conversion factor provided to determine the gain from the yield provided in photoelectrons. Our shadow-corrected data are compatible with the original model as well as the data of Qi et al., albeit with a systematic offset. However, there is tension with the measurements by Aprile et al., which also appear to be in conflict with

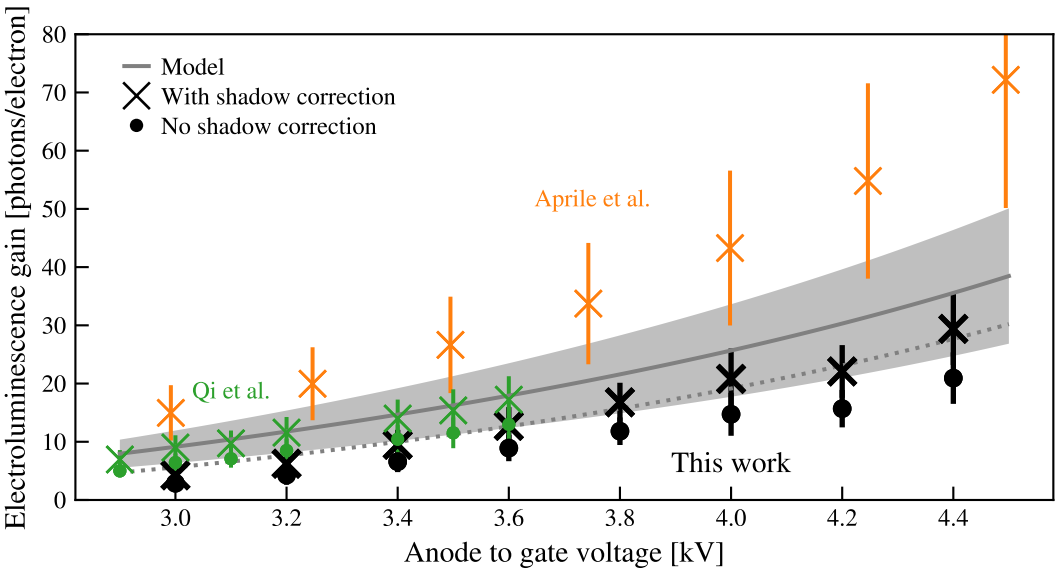

Figure 11. Comparison of our measured electroluminescence gain (black) to similar data from Qi et al. [20] (green) and Aprile et al. [18] (orange). The model from [18] applied to our electric field configuration is also shown (solid gray line with uncertainty band). Crosses indicate the shadow corrected, emitted electroluminescence gain, dots indicate the uncorrected, detectable gain. The data of Aprile et al. are based on a measurement using only the bottom PMT and are therefore considered to be shadow corrected.

their own model over this ΔV_{ag} range. Their results cover a larger range of anode voltages and the measurements at higher ΔV_{ag} constrain the model and produce this tension.

4.3 S2 resolution

The S2 resolution plays a role in the energy resolution of LXe TPCs and their ability to perform particle identification. Here, we study the impact of the single-phase technology on the resolution. For both $^{83\mathrm{m}}$Kr lines and all ΔV_{ag} values, the S2 area distributions are fitted by a Gaussian function with mean μ and standard deviation σ to obtain the energy resolution σ/μ and its uncertainty

$$\sigma^2_{\frac{\sigma}{\mu}} = \frac{\sigma^2_\sigma}{\mu^2} + \frac{\sigma^2\sigma^2_\mu}{\mu^4} + \frac{-\sigma \mathrm{cov}_{\mu\sigma}}{\mu^3}. \tag{4.4}$$

Here σ_i denotes the uncertainty of the variable i obtained from the fit. The resolution as a function of ΔV_{ag} are shown in Figure 12. Over the ΔV_{ag} range studied here, the resolution of the 32.1 keV decay's S2 deteriorates by 29%, reaching (34.2 ± 1.5) % at $\Delta V_{\mathrm{ag}} = 4.4$ kV. The resolution of the 9.4 keV decay deteriorates by 20%, reaching (46.3 ± 1.8) %. This trend could be caused by the increased electron multiplication and corresponding fluctuations. According to the model from [18], there is negligible electron multiplication at the lowest anode voltages, increasing to multiplication by a factor of about 1.4 at 4.4 kV.

4.4 Duration of the secondary electroluminescence signals and electron diffusion

The duration of the dual-phase S2 signal is driven by electron diffusion and the multi-millimeter path over which the secondary light is created. The duration of the single-phase S2 signal is dominated

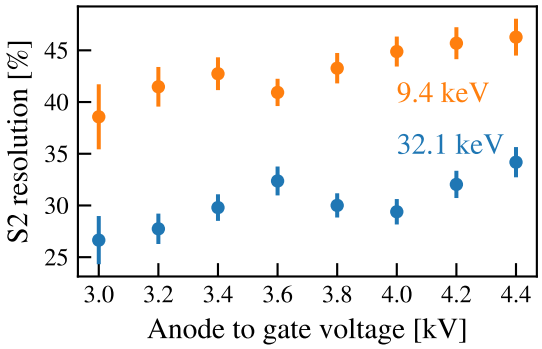

Figure 12. Single-phase S2 resolution for the different ΔV_{ag} and both ^{83m}Kr decays. Although the signal size increases with increasing ΔV_{ag}, the resolution worsens.

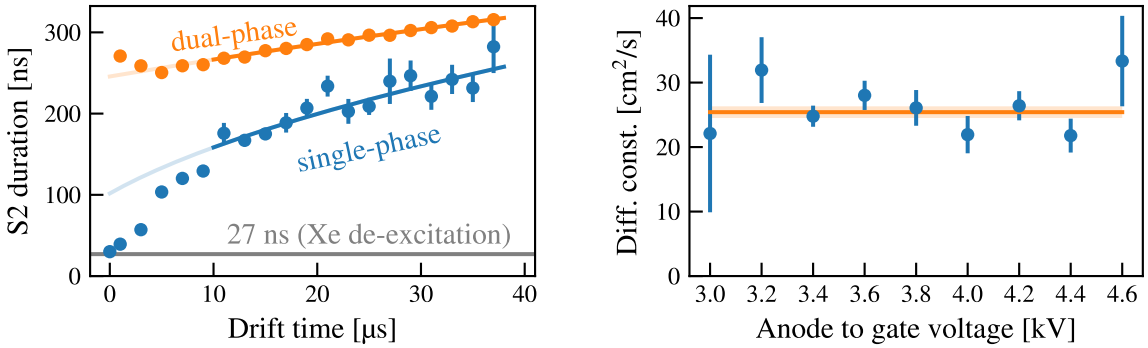

Figure 13. **Left:** Comparison of the S2 durations measured in single-phase (ΔV_{ag} = 4.0 kV) and dual-phase mode [21] as a function of the drift time. A fit to the data is performed in the range from 10 µs to 38 µs to extract the electron diffusion constants. The duration of the single phase S2 signals is dominated by diffusion for drift times above about 5 µs, but approaches the xenon de-excitation timescale for shorter drift times. The deviation from the fit seen at short drift times is due to non-uniformity of the electric field near the gate electrode. **Right:** The longitudinal diffusion constant D_L does not depend on ΔV_{ag}, as expected.

by diffusion and, for short drift times, the triplet de-excitation time of 27 ns of the Xe_2^* excimers. An example for ΔV_{ag} = 4.0 kV is shown in Figure 13, left, together with the data from operating the same TPC in dual-phase mode [21]. The single-phase S2 signals are significantly shorter than the dual-phase signals; at low drift times they approach the xenon de-excitation timescale. Only at drift times beyond the maximal drift time in this TPC would the duration be dominated by electron diffusion in both types of detector and then be comparable.

To obtain the longitudinal electron diffusion constant, the measured S2 duration w is plotted against the event's drift time and fitted by the diffusion formula

$$w = \sqrt{\frac{2D_L t}{v_{\text{drift}}^2} + w_0^2}. \tag{4.5}$$

The fit is restricted to the central part of the TPC, with drift times from 10 µs to 38 µs. This is the region with a homogeneous drift field and therefore a constant drift velocity. For the single-phase data, this fit was performed for all ΔV_{ag}; the results are shown in Figure 13, right. As

expected, the diffusion constant does not depend on ΔV_{ag}. The average longitudinal diffusion constant $D_L = (25.4 \pm 0.9)\,\mathrm{cm}^2/\mathrm{s}$ is compatible with the $(25.7 \pm 4.5)\,\mathrm{cm}^2/\mathrm{s}$ measured by Njoya et al. at 500 V/cm [38], but slightly higher than the $(19.5 \pm 0.6)\,\mathrm{cm}^2/\mathrm{s}$ obtained by Hogenbirk et al. at 490 V/cm [39].

4.5 S1 and S2 signal identification

For the results in this work, the S1 and S2 signals can be distinguished based on their time order within the unique ^{83m}Kr signature. For more general applications, however, a different classification method is required, that does not depend on the signal area. This can be achieved by exploiting the different underlying production processes, leading to different S1 and S2 signal shapes. S1s show a very steep rise followed by an exponential fall, while S2s have a more symmetric shape, where rise and fall times are similar. Here, we use the fall-time to rise-time ratio

$$\mathcal{R} = \frac{t_{90} - t_{50}}{t_{50} - t_{10}}, \tag{4.6}$$

where t_p is the time by which p% of the peak's area has been recorded. Figure 14, left shows the distribution of the ratio $\mathcal{R}$ for the four ^{83m}Kr decays. The discrimination power between S1s and S2s, defined by the fraction of peaks assigned the correct category, can be seen in Figure 14, right. It rises from around 40% at short drift times to above 80% for drift times longer than about 5 µs, where diffusion plays a greater role. It also improves with increasing signal size. This figure shows data for the rather low $\Delta V_{ag} = 3.4$ kV, but the discrimination is not significantly affected by ΔV_{ag}.

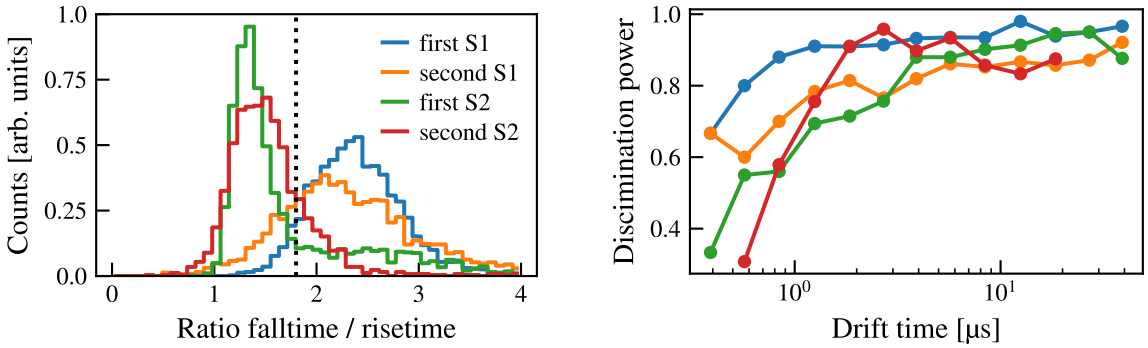

Figure 14. **Left:** The ratio of fall-time to rise-time for S1s and S2s at an anode voltage $\Delta V_{ag} = 4.4$ kV for ^{83m}Kr decays with a drift time between 1 µs and 2 µs. A ratio of 1.8 was used to split the regimes (dotted line). **Right:** The discrimination power increases with the drift time and the signal size. Shown here is data for the rather low $\Delta V_{ag} = 3.4$ kV; the discrimination power does not seem to depend on ΔV_{ag}.

5 Conclusions

Using proportional scintillation in LXe to measure the charge signal in TPCs could mitigate several construction and operation challenges, mainly related to the electrodes and the TPC's long-term stability. It would mitigate delayed electron extraction, allow for new analysis methods such as electron counting [13], and enable different detector designs such as radial drift [12, 20].

In this work, we have demonstrated that a single-phase TPC can be successfully operated, characterized and analyzed analogously to dual-phase TPCs. The design of our TPC that closely follows the dual-phase design employed successfully in a large number of dark matter experiments: a cylindrical TPC with 1:1 aspect ratio and light readout above and below the target. Since the small-scale TPC used for this study was previously operated in dual-phase mode [21], a direct comparison between the two signal generation processes was possible. The high electric fields required to generate proportional scintillation in the liquid phase were established around thin gold-plated tungsten anode wires of 10 µm diameter, by establishing a voltage difference ΔV_{ag} between the anode and the gate electrodes. Proportional scintillation from $^{83\mathrm{m}}$Kr calibration events was observed for $\Delta V_{\mathrm{ag}} \geq 3.0\,\mathrm{kV}$. Above 4.4 kV spontaneous light emission in the TPC prevented stable operation, as also observed in [40]. At the highest stable ΔV_{ag} of 4.4 kV, a scintillation gain of $g_2 = (1.9 \pm 0.3)$ PE/electron was achieved, which corresponds to an electroluminescence gain of (29 ± 6) photons/electron. The observed ΔV_{ag}-dependence is comparable to that reported in [20]. It is also compatible with the model proposed in [18], however, it might hint at a slightly higher electroluminescence threshold.

The maximum proportional scintillation gain factor g_2 achieved in the single-phase TPC is lower than the (5.49 ± 0.05) PE/electron achieved during dual-phase operation, with an extraction field (in the LXe) of 2.8 kV/cm [21]. It is also significantly lower than the gains achieved in large dual-phase TPCs searching for dark matter, with g_2 values of (16.5 ± 0.6) PE/electron in XENONnT [6], (28.8 ± 0.1) PE/electron in XENON1T [7] and (47.1 ± 1.1) PE/electron in LZ [8]. Since the S2 size impacts the rejection of electronic recoil backgrounds, higher single-phase g_2 gains would be needed to consider this technology as an alternative to the dual-phase TPC. Achieving higher gains will require improving our understanding of the spontaneous light emission and ways in which it can be reduced.

Using data from our single-phase TPC, we measured the electron drift velocity and the longitudinal electron diffusion constant at a drift field of 473 V/cm, with values in agreement with measurements in dual-phase TPCs. We have shown that single phase S2 signals can be used for three-dimensional position reconstruction and target fiducialization. Their duration is dominated by electron diffusion. This leads to narrower peaks at shorter drift times, potentially enabling new analysis techniques such as electron counting, and improving the identification of multiple S2 peaks in an event, which directly benefits background rejection in rare event searches.

Acknowledgments

This work was supported by the European Research Council (ERC) grant No. 724320 (ULTIMATE). We thank the teams of the mechanical and electronics workshops of the Institute of Physics, Freiburg, for their continuous support. Finally, we thank all the Bachelor students and interns who contributed to commissioning and operation of the detector, as well as data analysis.

References

[1] J. Billard et al., *Direct detection of dark matter – APPEC committee report*, *Rep. Prog. Phys.* **85** (2021) 056201, [2104.07634].

[2] PandaX-4T collaboration, Y. Meng et al., *Dark matter search results from the PandaX-4T commissioning run*, *Phys. Rev. Lett.* **127** (2021) 261802, [2107.13438].

[3] XENON collaboration, E. Aprile et al., *Projected WIMP sensitivity of the XENONnT dark matter experiment*, *J. Cosmol. Astropart. Phys.* **2020** (2020) 031, [2007.08796].

[4] LUX-ZEPLIN collaboration, D. Akerib et al., *The LUX-ZEPLIN (LZ) experiment*, *Nucl. Instrum. Meth. A* **953** (2020) 163047, [1910.09124].

[5] M. Schumann, *Dual-phase liquid xenon detectors for dark matter searches*, *JINST* **9** (2014) C08004, [1405.7600].

[6] XENON collaboration, E. Aprile et al., *Search for new physics in electronic recoil data from XENONnT*, *Phys. Rev. Lett.* **129** (2022) 161805, [2207.11330].

[7] XENON collaboration, E. Aprile et al., *Emission of single and few electrons in XENON1T and limits on light dark matter*, *Phys. Rev. D* **106** (2022) 022001, [2112.12116].

[8] LUX-ZEPLIN collaboration, J. Aalbers et al., *Search for new physics in low-energy electron recoils from the first LZ exposure*, *Phys. Rev. D* **108** (2023) 072006, [2307.15753].

[9] XENON collaboration, E. Aprile et al., *The XENON1T dark matter experiment*, *Eur. Phys. J. C* **77** (2017) 881, [1708.07051].

[10] XENON100 collaboration, E. Aprile et al., *The XENON100 dark matter experiment*, *Astropart. Phys.* **35** (2012) 573, [1107.2155].

[11] DarkSide collaboration, P. Agnes et al., *First results from the DarkSide-50 dark matter experiment at Laboratori Nazionali del Gran Sasso*, *Phys. Lett. B* **743** (2015) 456–466, [1410.0653].

[12] T. Ye, K. L. Giboni and X. Ji, *Initial evaluation of proportional scintillation in liquid xenon for direct dark matter detection*, *JINST* **9** (2014) P12007.

[13] F. Kuger et al., *Prospects of charge signal analyses in liquid xenon TPCs with proportional scintillation in the liquid phase*, *JINST* **17** (2021) P03027, [2112.11844].

[14] XENON collaboration, E. Aprile et al., *First dark matter search with nuclear recoils from the XENONnT experiment*, *Phys. Rev. Lett.* **131** (2023) 041003, [2303.14729].

[15] DARWIN collaboration, L. Althueser et al., *GPU-based optical simulation of the DARWIN detector*, *JINST* **17** (jul, 2022) P07018, [2203.14354].

[16] A. Lansiart et al., *Development research on a highly luminous condensed xenon scintillator*, *Nucl. Instrum. Meth.* **135** (1976) 47–52.

[17] K. Masuda et al., *A liquid xenon proportional scintillation counter*, *Nucl. Instrum. Meth.* **160** (1979) 247–253.

[18] E. Aprile et al., *Measurements of proportional scintillation and electron multiplication in liquid xenon using thin wires*, *JINST* **9** (2014) P11012, [1408.6206].

[19] Q. Lin, *Proposal of a Geiger-geometry single-phase liquid xenon Time Projection Chamber as potential detector technique for dark matter direct search*, *JINST* **16** (2021) P08011, [2102.06903].

[20] J. Qi et al., *Low energy electronic recoils and single electron detection with a liquid xenon proportional scintillation counter*, *JINST* **18** (2023) P07027, [2301.12296].

[21] D. Baur et al., *The XeBRA platform for liquid xenon time projection chamber development*, *JINST* **18** (2023) T02004, [2208.14815].

[22] XENON collaboration, E. Aprile et al., *The triggerless data acquisition system of the XENONnT experiment*, *JINST* **18** (2023) P07054, [2212.11032].

[23] P. Zappa et al., *A versatile and light-weight slow control system for small-scale applications*, *JINST* **11** (sep, 2016) T09003–T09003, [1607.08189].

[24] A. Manalaysay et al., *Spatially uniform calibration of a liquid xenon detector at low energies using* ^{83m}Kr, *Rev. Sci. Instrum.* **81** (2010) 073303, [0908.0616].

[25] L. W. Kastens et al., *A* $^{83}Kr^{m}$ *source for use in low-background liquid xenon time projection chambers*, *JINST* **5** (2010) P05006, [0912.2337].

[26] J. Aalbers et al., *AxFoundation/strax: v0.6.1*, 2019. 10.5281/zenodo.2544792.

[27] R. Saldanha et al., *Model independent approach to the single photoelectron calibration of photomultiplier tubes*, *Nucl. Instrum. Meth. A* **863** (2017) 35–46, [1602.03150].

[28] F. G. Kondev, M. Wang, W. J. Huang, S. Naimi and G. Audi, *The NUBASE2020 evaluation of nuclear physics properties*, *Chinese Phys. C* **45** (2021) 030001.

[29] A. Bismark, *Simulation and characterization of a LXe TPC for DARWIN R&D*. Master's thesis, *U. Freiburg*, 2019.

[30] GEANT4 collaboration, S. Agostinelli et al., *GEANT4—a simulation toolkit*, *Nucl. Instrum. Meth. A* **506** (2003) 250–303.

[31] M. Abadi et al., *TensorFlow: Large-scale machine learning on heterogeneous systems*, 2015. tensorflow.org.

[32] F. Chollet et al., *Keras*, 2015. keras.io.

[33] F. Jörg et al., *Characterization of alpha and beta interactions in liquid xenon*, *Eur. Phys. J. C* **82** (2022) 361, [2109.13735].

[34] C. E. Dahl, *The physics of background discrimination in liquid xenon, and first results from XENON10 in the hunt for WIMP dark matter*. PhD thesis, *Princeton U.*, 2009.

[35] L. Baudis et al., *Response of liquid xenon to Compton electrons down to 1.5 keV*, *Phys. Rev. D* **87** (2013) 115015, [1303.6891].

[36] A. G. Singh et al., *Analysis of* ^{83m}Kr *prompt scintillation signals in the PIXeY detector*, *JINST* **15** (2020) P01023, [1911.03999].

[37] G. Martinez-Lema et al., *First observation of liquid xenon electroluminescence with a microstrip plate*, *JINST* **19** (2024) P02037, [2312.14663].

[38] O. Njoya et al., *Measurements of electron transport in liquid and gas xenon using a laser-driven photocathode*, *Nucl. Instrum. Meth. A* **972** (2020) 163965, [1911.11580].

[39] E. Hogenbirk, M. P. Decowski, K. McEwan and A. P. Colijn, *Field dependence of electronic recoil signals in a dual-phase liquid xenon time projection chamber*, *JINST* **13** (2018) P10031, [1807.07121].

[40] Y. Wei, J. Qi, E. Shockley, H. Xu and K. Ni, *Performance of a radial time projection chamber with electroluminescence in liquid xenon*, *JINST* **17** (2022) C02002, [2111.09112].